frontiers | Frontiers in Earth Science

TYPE Original Research
PUBLISHED 17 August 2022
DOI 10.3389/feart.2022.961311

OPEN ACCESS

EDITED BY
Maxim Lebedev,
Curtin University, Perth, Australia

REVIEWED BY
Xiangxin Liu,
North China University of Science and Technology, China
Hemin Yuan,
China University of Geosciences, China

*CORRESPONDENCE
Xinxin Fang,
fx15827573109@163.com

SPECIALTY SECTION
This article was submitted to Solid Earth Geophysics, a section of the journal Frontiers in Earth Science

RECEIVED 04 June 2022
ACCEPTED 18 July 2022
PUBLISHED 17 August 2022

CITATION
Fang X, Feng H, Wang Y and Fan T (2022), Prediction method and distribution characteristics of in situ stress based on borehole deformation—A case study of coal measure stratum in Shizhuang block, Qinshui Basin.
Front. Earth Sci. 10:961311.
doi: 10.3389/feart.2022.961311

Prediction method and distribution characteristics of *in situ* stress based on borehole deformation—A case study of coal measure stratum in Shizhuang block, Qinshui Basin

Xinxin Fang[1,2]*, Hong Feng[2], Yunhong Wang[2] and Tao Fan[2]

[1]China Coal Research Institute, Beijing, China, [2]China Coal Technology & Engineering Group Xi'an Institute, Xi'an, China

A geometric equation of borehole deformation under stress was deduced based on the basic theory of elasticity. Subsequently, we established the quantitative relationship between the *in situ* stress and geometrical parameters of borehole deformation. Furthermore, we proposed an *in situ* stress prediction model based on borehole deformation. Additionally, numerical simulations of borehole morphology in different lithologies under *in situ* stress were conducted to analyze the deformation effect. Logging parameters that are sensitive to the shear wave time difference, such as longitudinal wave time difference, density, and natural gamma radiation, were selected for training using an artificial neural network (ANN) to predict the shear wave time difference. The results demonstrated that 1) combining the theoretical derivation and numerical simulation, the borehole geometry under stress was quasi-elliptic, and 2) compared with the existing shear wave time difference curve, the predicted geometry by the ANN was consistent with the actual geometry. Consequently, compared with the tested data from acoustic emission, the overall error of the *in situ* stress predicted using the new method was less than 9.2%. Moreover, the accuracy of the coal seam was the highest, wherein the average errors of the maximum and minimum horizontal principal stresses were 2.01 and 2.56%, respectively, which confirms the feasibility of the proposed method.

KEYWORDS

***in situ* stress, borehole deformation, ANN, coal measure stratum, Qinshui Basin**

1 Introduction

In situ stress is the natural stress existing in the stratum undisturbed by engineering, also known as the initial stress of rock mass or original rock stress. *In situ* stress analysis can intuitively reflect the variation law of *in situ* stress field in vertical and plane and provide basic information for drilling engineering and oil and gas reservoir development (Daniel and Christoph, 2016; Farshid et al., 2020; Zhang et al., 2021; Yang et al., 2022). It is an important reference for the selection of perforating and fracturing scale and parameters and prediction of sand production in production layers (Zou and Kaiser, 1990; Feng et al., 2019; Ju et al., 2020). *In situ* stress is the fundamental force that causes deformation and failure of mining and other underground engineering; in addition, its magnitude and direction have a great influence on the stability of the surrounding rock. Measurement of *in situ* stress is a necessary prerequisite for determining the mechanical properties of engineering rock mass, analyzing the stability of the surrounding rock, and implementing the scientific design of underground engineering excavation.

With the development of oil and gas theory, continuous exploration and development, unconventional resources, such as coalbed methane, shale oil, and gas, and tight oil and gas, show great potential under the existing technical conditions. China is rich in CBM resources, but the physical properties of coal seams are poor and the development is difficult. As fracturing is one of the key technologies to complete the effective production of CBM, the *in situ* stress distribution of reservoirs is a necessary parameter for the design of the fracturing process (Bell, 2006; Ju et al., 2017; Liu et al., 2021; Shi et al., 2021). *In situ* stress controls every link in the process of coalbed methane reservoir formation. It is the most important factor affecting the permeability of coal seam and also an important parameter that must be considered in the fracturing design and well pattern deployment of coalbed methane wells. Recently, with the increasing development of coalbed methane resources, it is extremely urgent to develop accurate and continuous *in situ* stress prediction methods for coalbed methane industry. However, compared with conventional natural gas, the study of *in situ* stress in the research and development of coalbed methane is relatively weak. It is of great practical significance to explore the distribution law and influencing factors of *in situ* stress in coalbed methane fields for coalbed methane exploration, development, and safe production.

In situ stress data can usually be obtained by testing, fracturing, or calculation. Test is the most direct means. Presently, more and more testing and calculation methods are available (Ishida and Saito, 1995; Cai et al., 2006; Hikweon and See, 2018). However, much difficulty exists, such as expensive cost, limited data acquisition, and the discontinuous profile of *in situ* stress. *In situ* stress measurement methods can be divided into three categories: 1) mechanical method based on the determination of strain and deformation in rock mass, such as stress recovery, stress relief, and hydraulic fracturing; 2) the geophysical method based on the measurement of acoustic emission, acoustic wave propagation law, resistivity, or other physical parameters in rock mass; and 3) determining the stress direction according to the information provided by the geological structure and underground rock mass failure. Presently, hydraulic fracturing and acoustic emission are widely used in petroleum and coal methane production (Atsushi et al., 2007; Wang and Zhang, 2018; Yang et al., 2021). The operation of hydraulic fracturing is simple and adaptable, whereas it is limited by the discontinuous data and expensive cost, and time-consuming nature. The acoustic emission method is a more accurate test method in the laboratory, which needs to rely on a large amount of core data, whereas it is limited by *in situ* stress data (Khair et al., 2013; Huffman et al., 2016). Therefore, considering the difficulty and cost of current methods, the author proposes an *in situ* stress prediction method based on the borehole deformation geometry and logging data to achieve continuous and accurate *in situ* stress prediction in the study area.

Borehole will be deformed to some extent by the action of stress. The geometry of the borehole after deformation reflects the stress characteristics of the borehole wall. Many studies have been carried out on borehole deformation under *in situ* stress. Kirsch (1898) proposed the Kirsch solution of rock mass stress and aperture deformation around the borehole, which laid the theoretical foundation of the *in situ* stress measurement method based on aperture deformation. Zoback et al. (1985) statistically analyzed the relationship between the borehole collapse pattern caused and *in situ* stress. Haison and Herrick (1985) conducted experimental research based on Zoback's theory and proposed that borehole deformation is directly related to the stress state. Wang and Pan (1991) analyzed the borehole deformation under planar and three-dimensional stress states and derived the solution formula of displacement of borehole wall under two stress states. Peska and Zoback (1995) studied the effect of tensile strength of the surrounding rock on borehole deformation during drilling. Jaeger et al. (2009) derived the analytical solution of the displacement of the hole wall of a circular hole under far-field stress. According to Gough and Bell, the elliptical borehole is caused by shear fracture in the stress concentration zone near the borehole wall, with the long axis in the same direction as the minimum horizontal principal stress (Xu et al., 2016). The abovementioned scholars have studied the relationship between borehole displacement and *in situ* stress theoretically, but they have not studied the geometric morphology characteristics of borehole under stress and the prediction of *in situ* stress by borehole geometric morphology parameters after deformation.

Based on the analysis of the problems existed in the measurement of *in situ* stress, we deduced the geometric morphology equation of borehole under the action of stress

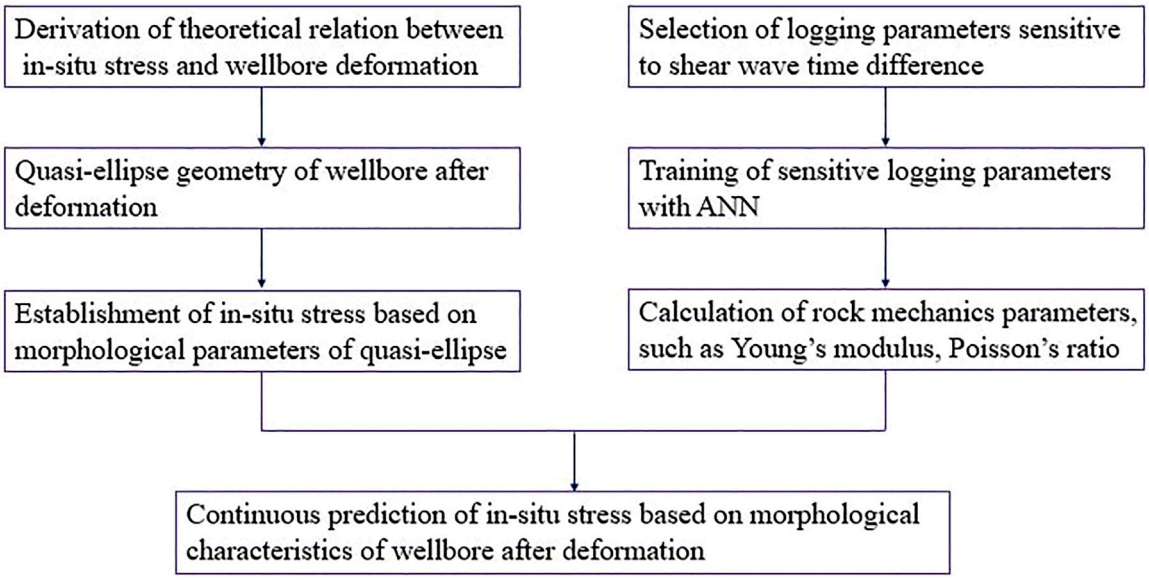

FIGURE 1
Continuous *in situ* stress prediction flow chart based on borehole deformation characteristics.

theoretically and then confirmed that the shape of a borehole after deformation is quasi-elliptic. Subsequently, we established the *in situ* stress prediction model based on quasi-elliptic geometric parameters. Finally, we formed the *in situ* stress prediction method based on borehole deformation. Considering the lack of shear wave time difference (DTS), we selected the longitudinal wave time difference (DTC), density (DEN), and natural gamma (GR) that are sensitive to shear wave time difference and then established the prediction model of shear wave time difference (DTS) by training these sensitive logging parameters with an artificial neural network (ANN) to obtain the rock mechanics parameter model, namely, Young's modulus (E) and Poisson's ratio (ν). The method proposed in this study is applied to the coal measure strata of Qinshui Basin to obtain the *in situ* stress distribution of the No. 3 and No. 15 coal seams and then analyze the effect of *in situ* stress on the permeability of coal seams. The overall idea of this study is shown in Figure 1.

2 Geological setting

Qinshui Basin is located in the southeast of Shanxi Province, with a latitude of 35°–38° N and a longitude of 110°00′ – 113°50′ N (Fu et al., 2017; Wang et al., 2017; Wu et al., 2020). It generally extends along the NNE direction in a long axis shape and shrinks into an ellipse in the middle. The coal-bearing strata in Qinshui Basin are mainly distributed in the Taiyuan formation of upper Carboniferous and Shanxi Formation of Lower Permian, which are a set of coal-bearing facies transition deposits developed on the Ordovician weathering crust. The Taiyuan Formation is mainly a coastal carbonate platform sedimentary system. The Shanxi Formation is mainly a fluvial delta sedimentary system. Qinshui Basin is one of the areas with the highest degree of coalbed methane exploration and development in China. The main coal seams are the No. 3 coal seam of the Shanxi Formation and the No. 15 coal seam of the Taiyuan Formation (Liu et al., 2014). The studied area is located in the south of Qinshui Basin (Figure 2). The buried depth of the No. 3 coal seam is 580–1830m. The buried depth of the No. 15 coal seam is about 200 m larger than that of the No. 3 coal seam.

3 Methods

3.1 Derivation of the theoretical relationship between *in situ* stress and borehole deformation

3.1.1 Borehole deformation under *in situ* stress

Figure 3 is a schematic diagram of the cross section of the borehole. A hole of a circular cross-section is drilled with radius r into the formation. The formation is assumed to be infinite and elastic, and the borehole is subjected to far-field stress. The stress is assumed to be positive in the direction of tension and negative in the direction of pressure, and the coordinate axes coincide with the direction of principal stress. In the X–Y coordinate system, the stress can be expressed as

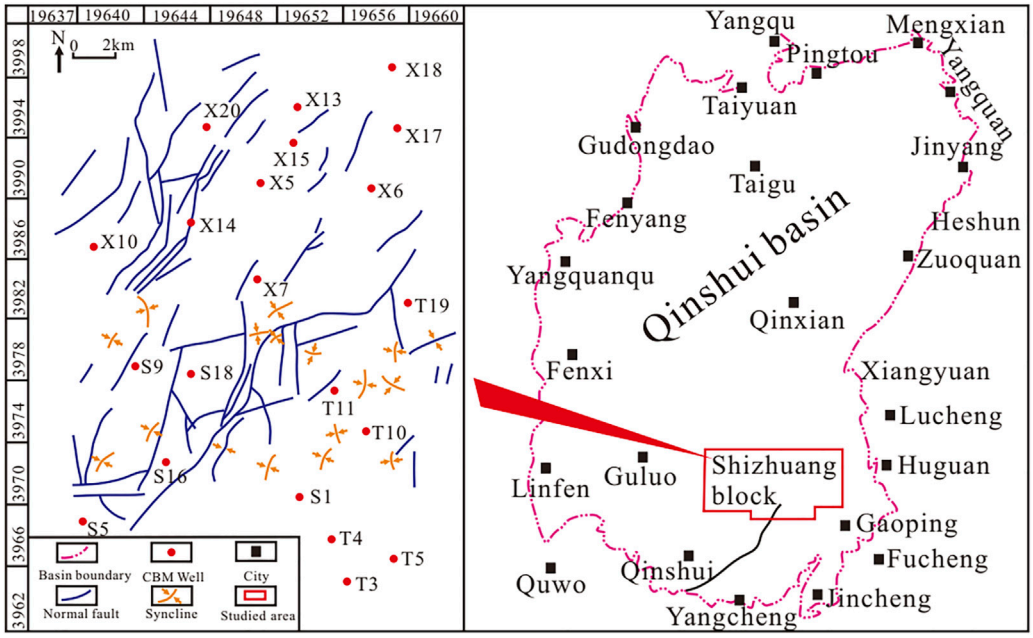

FIGURE 2
Structural topographic map of Qinshui Basin and the studied area.

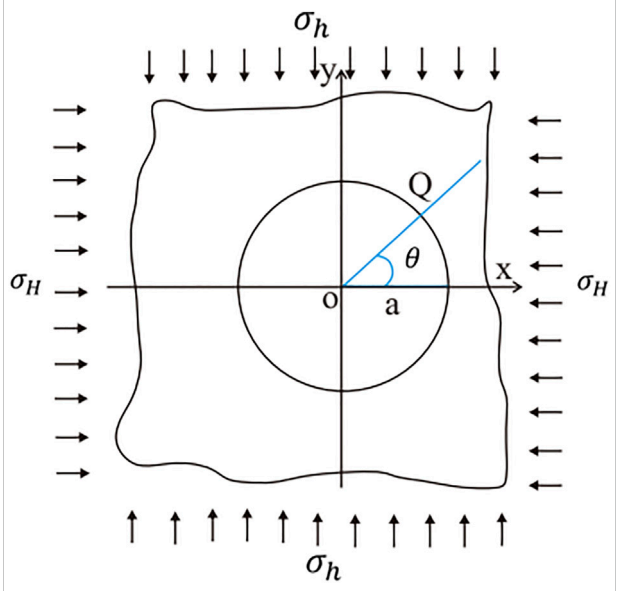

FIGURE 3
Schematic diagram of borehole displacement.

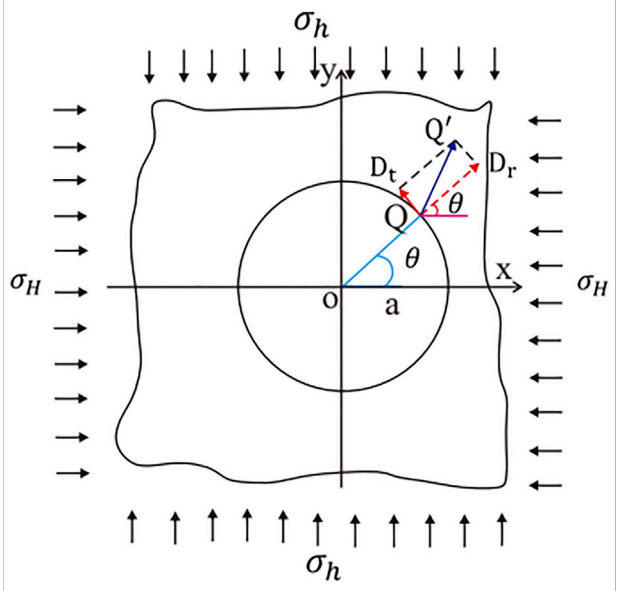

FIGURE 4
Changes at any point on the shaft wall.

$$\{\sigma\} = \{\sigma_H, \sigma_h\} \quad (1)$$

where σ_H– is the maximum horizontal principal stress, MPa, and σ_h– is the minimum horizontal principal stress, MPa.

According to the theory of elasticity, the radial displacement D_r and tangential displacement D_t of any point Q in the well hole are

$$\begin{cases} D_r = -\dfrac{(1-\nu^2)r}{E}\left[(\sigma_H+\sigma_h)+2(\sigma_H-\sigma_h)\cos 2\theta\right] \\ D_t = \dfrac{(1-\nu^2)r}{E}\left[2(\sigma_H-\sigma_h)\sin 2\theta\right] \end{cases}, \quad (2)$$

where E is Young's modulus (GPa), ν is Poisson's ratio, θ is the angle between the radial direction of point Q and the positive direction of X-axis, and r is the borehole radius.

3.1.2 Quasi-elliptic structure of the borehole under *in situ* stress

Assuming that point Q is deformed to point Q′ at the coordinates (x, y), as shown in Figure 4, then

$$\left.\begin{aligned} x &= a*\cos\theta + D_r*\cos\theta - D_t*\sin\theta \\ y &= a*\cos\theta + D_r*\sin\theta + D_t*\cos\theta \end{aligned}\right\}. \quad (3)$$

Substituting Eq. 2 into Eq. 3, after simplification, we obtain

$$\left.\begin{aligned} x &= a[1+(3\sigma_H-\sigma_h)/E]\cos\theta \\ y &= a[1+(3\sigma_h-\sigma_H)/E]\sin\theta \end{aligned}\right\}. \quad (4)$$

Let

$$\left.\begin{aligned} A_0 &= a[1+(3\sigma_H-\sigma_h)/E] \\ B_0 &= a[1+(3\sigma_h-\sigma_H)/E] \end{aligned}\right\}. \quad (5)$$

Then, Eq. 4 can be expressed as

$$\left.\begin{aligned} x &= A_0\cos\theta \\ y &= B_0\sin\theta \end{aligned}\right\}. \quad (6)$$

Equation 6 meets the following condition:

$$\frac{x^2}{A_0^2}+\frac{y^2}{B_0^2} = \cos^2\theta+\sin^2\theta = 1, \quad (7)$$

which is the standard ellipse equation. However, owing to the difference in the elastic modulus of rocks, A_0 and B_0 vary with the depth. Therefore, the geometric shape of the circular hole after deformation under the state of plane stress can be approximated as an ellipse, namely, quasi-elliptic structure. Theoretically, it is proven that the borehole morphological structure under stress is ellipse.

3.1.3 *In situ* stress prediction model based on quasi-elliptic borehole shape

Assuming that A and B are the lengths of major and minor semi-axes of quasi-ellipses, respectively, then when $A_0 > B_0$, namely, under tensile action, $A=A_0$ and $B=B_0$; when $A_0 < B_0$, namely, under compression, $A=B_0$ and $B=A_0$. We can solve σ_H and σ_h by the following equations:

$$\left.\begin{aligned} \sigma_H &= \frac{3A_0+B_0-4a}{8a}E \\ \sigma_h &= \frac{A_0+3B_0-4a}{8a}E \end{aligned}\right\}. \quad (8)$$

For the elliptic borehole, the direction of minimum horizontal principal stress is along the long axis of the ellipse. Dual caliper logs can be applied to determine the long and short axes of the ellipse (Figure 5). C13 corresponds to the long axis of the elliptical borehole. C24 corresponds to the short axis of the elliptic borehole.

Young's modulus E and Poisson's ratio ν are usually determined by the following equations:

$$E = \frac{DEN}{DTS^2}\cdot\frac{3DTS^2-4DTC^2}{DTS^2-DTC^2}, \quad (9)$$

$$\nu = \frac{0.5\times(DTS/DTC)^2-1}{(DTS/DTC)^2-1}, \quad (10)$$

where DEN is the formation density, g/cm^3; DTS is the shear wave time difference, μs · m^{-1}; E is Young's modulus, GPa; and ν is Poisson's ratio.

Density (DEN) and longitudinal wave time difference (DTC) are two parameters that can be obtained directly from conventional logging. Shear wave time difference (DTS) is not available in all wells. It is usually predicted with existing logging parameters. In this study, the artificial neural network is selected to train sensitive logging parameters to predict the shear wave time difference.

3.2 Prediction of shear wave time difference with artificial neural network

Artificial neural network (ANN) is a powerful tool applied in the computer field to deal with machine learning problems. It is widely applied in regression and classification issues (Husken et al., 2005; Deng et al., 2006; Lin et al., 2021; Fang et al., 2022). It consists of a large number of simple processing units called neurons and is developed by imitating the behavior of the human brain. Same as the human brain, the neural network collects information from the environment by "learning process", forms a network structure of artificial neurons with hierarchical and connection relationship, and then simulates the signal transmission between neurons by a mathematical expression, thereby establishing a nonlinear equation with input and output relationship as well as being visualized by the network, which is called the ANN. Generally speaking, the ANN can fit any nonlinear function through reasonable network structure configuration; thus, it is also applied to dispose nonlinear systems or black box models with a more complex internal expression (Lv et al., 2017; Behzad et al., 2019; Zhang et al., 2020).

3.2.1 Artificial neural network structure

The artificial neural network selected in this study is a multi-layer feedforward artificial neural network. Its structure is shown in Figure 6.

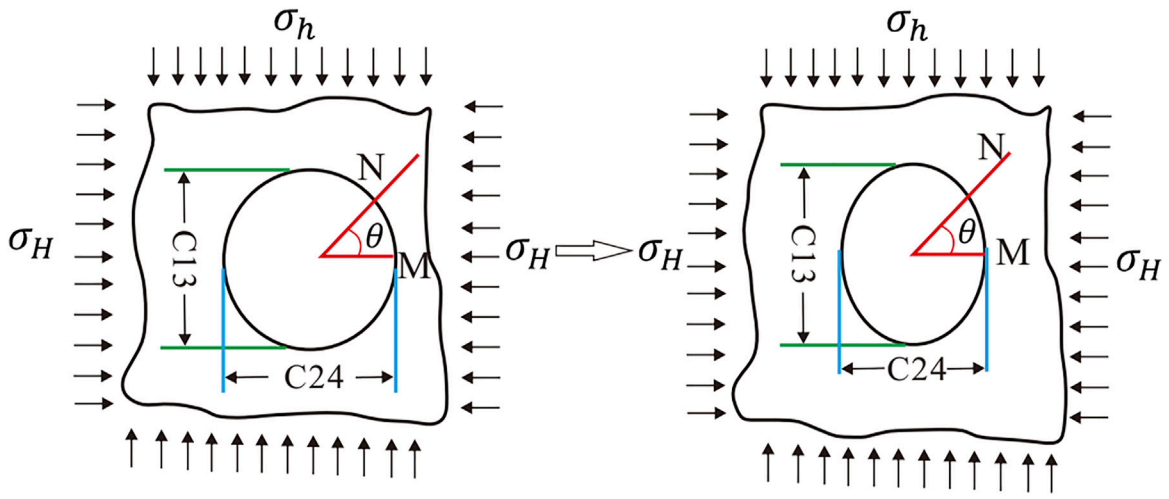

FIGURE 5
Diagram of the relation between long and short axes and diameters of the elliptic borehole.

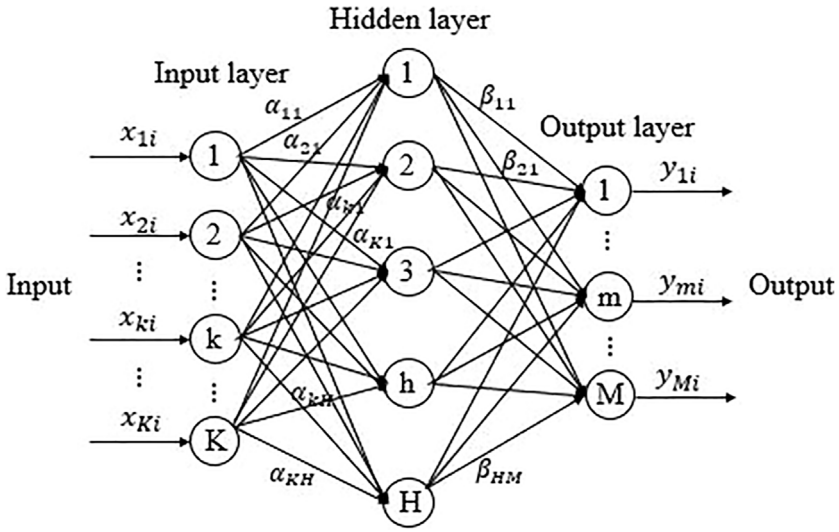

FIGURE 6
Multilayer feedforward neural network architecture.

The relationship between the input and output of the neural network above is shown in the following equation:

$$y_{mi} = S_2\left[\sum_{h=1}^{H}\beta_{hm}S_1\left(\sum_{k=1}^{K}\alpha_{kh}x_{ki} + \theta_{1h}\right) + \theta_{2m}\right], 1 \le m \le M, \quad (11)$$

where y_{mi} is the output of the *m*th neuron in the output layer for the *i*th training sample, xi = [x1i, x2i, ⋯, xki, ⋯, xKi] is the *i*th training sample, S_1 and S_2 are the activation functions of neurons in the hidden layer and output layer, respectively, β_{hm} is the activation for the *h*th neuron in the hidden layer to the *m*th neuron in the output layer, θ_{1h} and θ_{1m} are the threshold of the *h*th neuron in the hidden layer and the *m*th neuron in the output layer, respectively, and K, H, and M are the number of neurons in the input layer, the hidden layer, and the output layer, respectively. From a mathematical point of view, the multilayer feedforward neural network achieves a mapping from the input to output. As long as the number of hidden layer neurons is enough, the multilayer feedforward neural network can theoretically achieve any complex mapping.

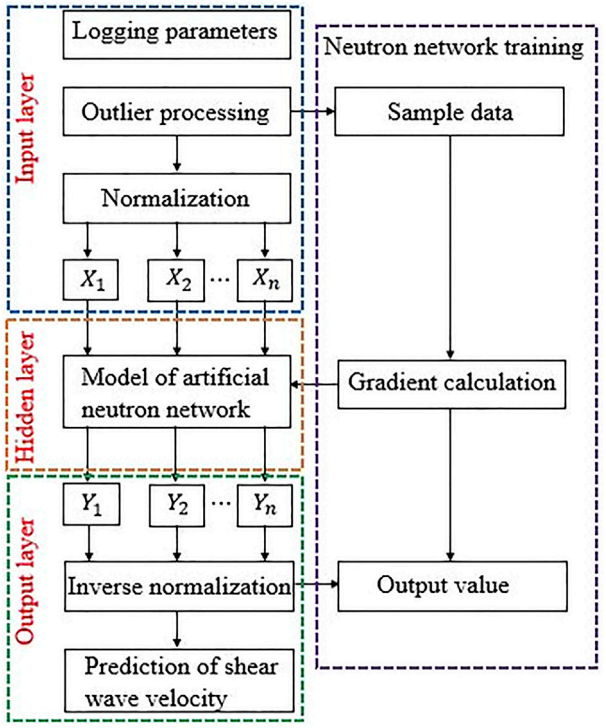

FIGURE 7
Prediction process of the shear wave time difference with the ANN.

Shear wave time difference prediction based on the artificial neural network is completed by selecting the logging parameters sensitive to the shear wave time difference as samples for learning and training and then gradually correcting the weight of each connection, namely, the weighted sum of the bias vector, thereby making the output of the network gradually approach the inherent true value.

3.2.2 Prediction of shear wave time difference based on the artificial neural network

The prediction process of the shear wave time difference based on the ANN is shown in Figure 7, which mainly consists of an input layer, a hidden layer, and an output layer. The input layer performs outlier processing and normalization (normalization can improve the speed and accuracy of neural network training) for logging parameters that have certain correlation with s-wave logging data. Its normalization formula is

$$X_i = (X_i - X_{\min})/(X_{\max} - X_{\min}), (i = 1, 2, \cdots, n), \quad (12)$$

where X_{min} and X_{max} are the minimum and maximum values of X_i, respectively. First, the processed data are input to the hidden layer. Then, the hidden layer receives the data and calculates with the neural network model. Subsequently, the calculated results are transmitted to the output layer. After that, the output layer receives the calculated results and conducts inverse normalization processing. Finally, the prediction of shear wave time differences is received.

In this study, three wells with complete logging data and shear wave time difference data were selected for analysis. It was found that a certain relationship between the shear wave time difference (DTS) and longitudinal wave time difference (DTC), natural gamma (GR), and density (DEN) existed with intersection analysis, as shown in Figure 8. Therefore, DTC, GR, and DEN were selected as the input of the training network of the shear wave time difference. Gradually, the weights of their connections were corrected. Subsequently, the relationship between them and the shear wave time difference trained with the neural network was approximated. Thereby, the predicted shear wave time difference approximating the real value is regarded as the output. Figure 9 shows the comparison between the predicted DTS and the measured ones in the training well. It can be seen that the predicted DTS is in line with the actual shear wave time difference, testifying that the prediction results are reliable.

3.3 Numerical simulation of borehole morphology under stress

The formation around the borehole is highly sensitive to stress, resulting in the borehole morphology being changed under stress. In the process of numerical simulation, it is assumed that the stratum around the hole is isotropic and homogeneous; in addition, under the action of uniform horizontal *in situ* stress, the studied issue is simplified as the plane strain ones. The geometric size of the model is designed as a square of 0.2 m × 0.2 m, with the aperture of hole 0.015 m (Figure 10). The rock physical parameters of the strata are shown in Table 1.

Mudstone, sandstone, coal, and limestone were selected in the numerical simulation. The maximum and minimum horizontal principal stress was set according to the compressive strength four types of rocks. It can be seen from Figure 11, within the scope of the compressive strength, the geometric morphology of the borehole under the maximum and minimum horizontal principal stress is an ellipse shape. The direction of the maximum horizontal principal stress is parallel with the short axis of the ellipse, which is consistent with the theoretical derivation. Affected by the influence of *in situ* stress, the deformation degree of the borehole wall of mudstone is larger than that of other lithologies; in addition, the deformation extent of limestone is the least. Therefore, it is further indicated that the maximum and minimum horizontal principal stresses can be predicted according to pore morphology characteristics.

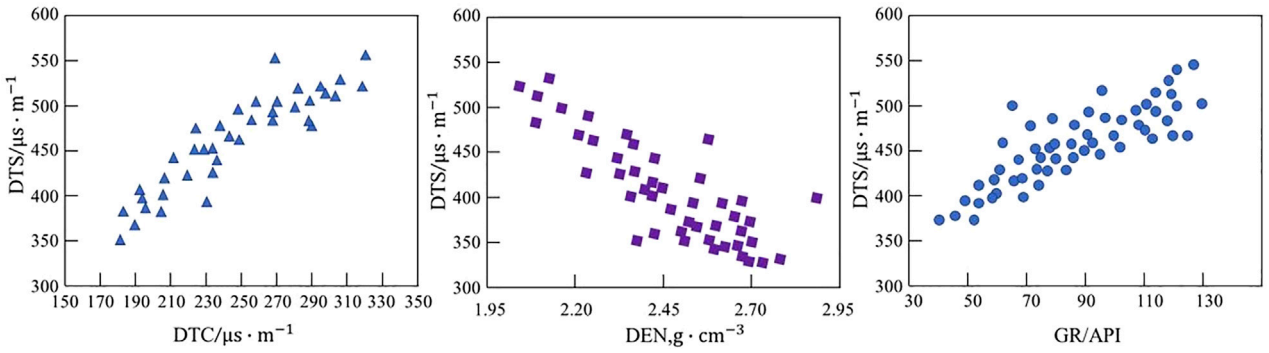

FIGURE 8
Cross plot of logging parameters and s-wave time difference (DTS).

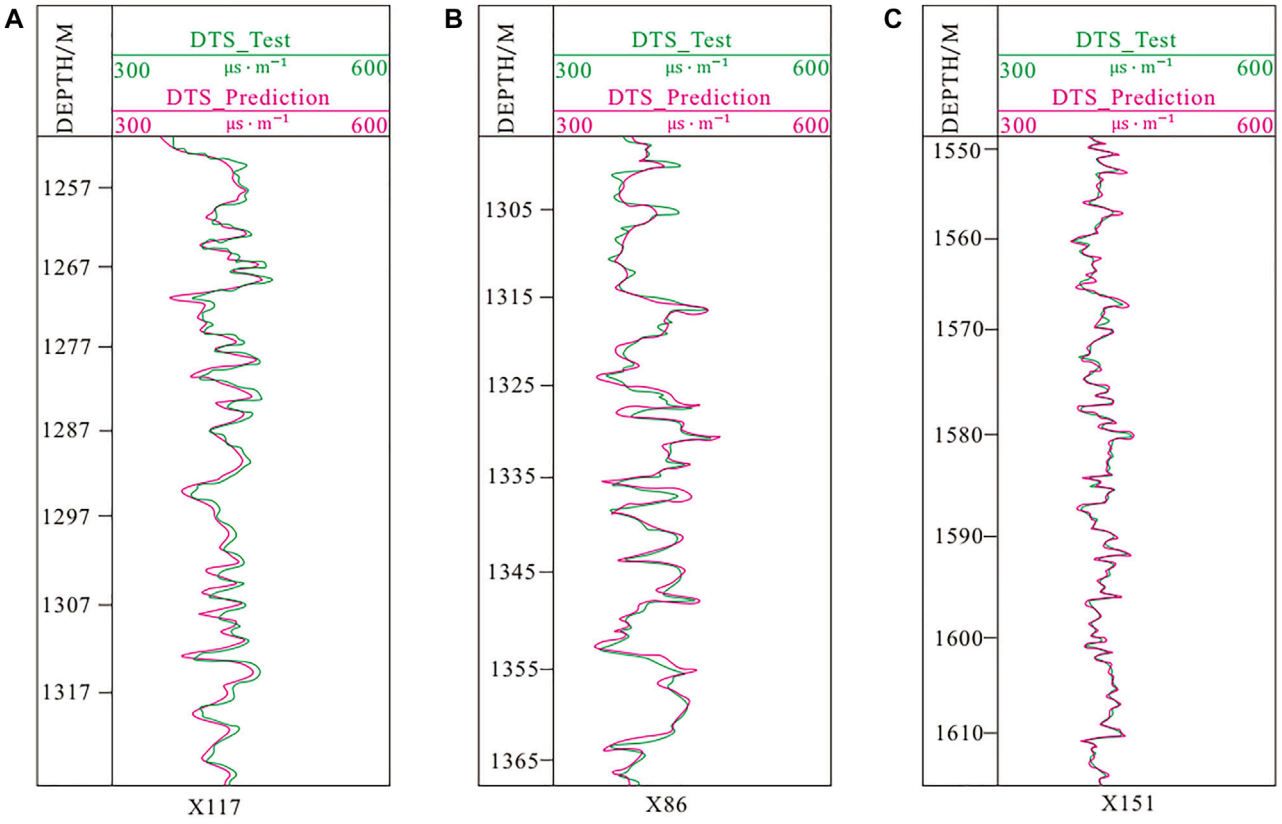

FIGURE 9
Comparison between the measured shear wave time difference and prediction in different wells.

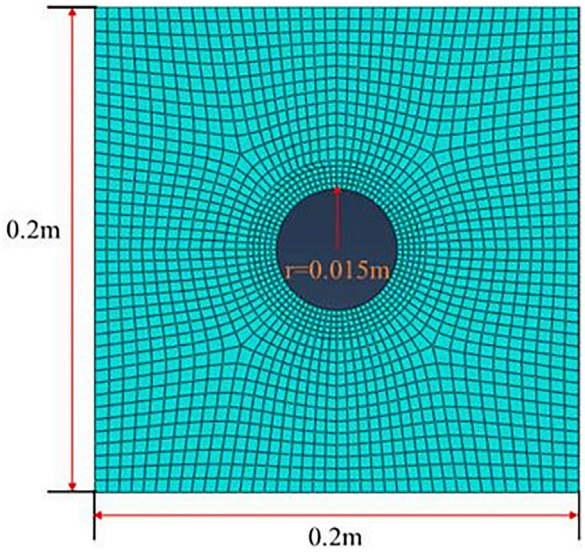

FIGURE 10
Grid structure of numerical simulation.

4 Results

4.1 Comparison of prediction and test

The method proposed in this study is applied to the S16 well to obtain the continuous profile of the maximum and minimum *in situ* stress in a single well (Figure 12). According to this profile (Figure 12), the maximum and minimum horizontal principal stress shows an increasing trend with depth; in addition, the maximum horizontal principal stress is greater than the minimum horizontal principal stress. The mean values of the maximum horizontal principal stress of mudstone, fine sandstone, gritstone, coal, and limestone are 21.8, 25.0, 26.3, 33.9, and 40.7 MPa, respectively. The mean values of the minimum horizontal principal stresses corresponding to these five lithologies are 18.1, 23.1, 23.9, 30.2, and 34.1 MPa, respectively. Based on the statistics on the azimuth of the long axis of the ellipse, it is exhibited that the azimuth of the long axis of the ellipse is 302°–319°; thus, the direction of the maximum principal stress is approximately N30^{0}E (Table 2).

By comparing the *in situ* stress predicted by the new method with acoustic emission data in the laboratory (Table 3), it can be found that the average error of the maximum horizontal principal stress is 6.1% and the average error of the minimum horizontal principal stress is 7.0%. The average error of the maximum horizontal principal stress predicted by the new method is greater than that of the minimum horizontal principal stress. In addition, the error of different lithologies is also different. The prediction errors of the maximum horizontal principal stress of mudstone, fine sandstone, gritstone, coal, and limestone are 5.82, 3.89, 3.27, 2.01, and 2.52%, respectively. The prediction errors of the minimum horizontal principal stress of these five lithologies are 8.36, 3.99, 2.53, 2.56, and 3.19%, respectively. The prediction error of the maximum and minimum horizontal principal stress of coal in five lithologies is the smallest. Generally, the average error of the new method is lower than 9.2%, which can meet the demand of production.

4.2 Distribution of maximum horizontal principal stress and differential stress

The new method was applied to predict the *in situ* stress of the coal seam in 15 wells of the study area. The plane distribution of the *in situ* stress and difference of horizontal principal stress ($\sigma_H - \sigma_h$) of No. 3 and No. 15 coal seams in the study area were obtained by combining the prediction data of a single well with regional geological characteristics (Figures 13, 14). It can be seen from Figures 13 and 14 that the range of the maximum horizontal principal stress in the No. 3 coal seam is 22.6–39 MPa; in addition, the range of horizontal principal stress difference is 2.1–7.1 MPa. The variation trend of the maximum horizontal principal stress and the difference of the horizontal principal stress of the No. 3 coal seam are higher in the east and lower in the west from west to east, with the maximum principal stress 40.2 MPa and the difference of horizontal principal stress ($\sigma_H - \sigma_h$) 7.1 MPa. The range of the maximum horizontal principal stress of the No. 15 coal seam is 20–43 MPa, and the distribution range of the horizontal principal stress difference is 1.8–8.8 MPa. The maximum horizontal principal stress is high in the east and low in the west; in addition, the maximum horizontal principal stress is 43.6 MPa. However, the

TABLE 1 Setting of petrophysical parameters.

Lithology	Young's modulus/GPa	Poisson's ratio	Density/g · cm^{-3}	Compressive strength/MPa
Mudstone	9.65	0.35	2.49	178.6
Sandstone	12.73	0.32	2.56	208.8
Coal	13.15	0.43	1.90	225.6
Limestone	30.25	0.21	2.79	355.6

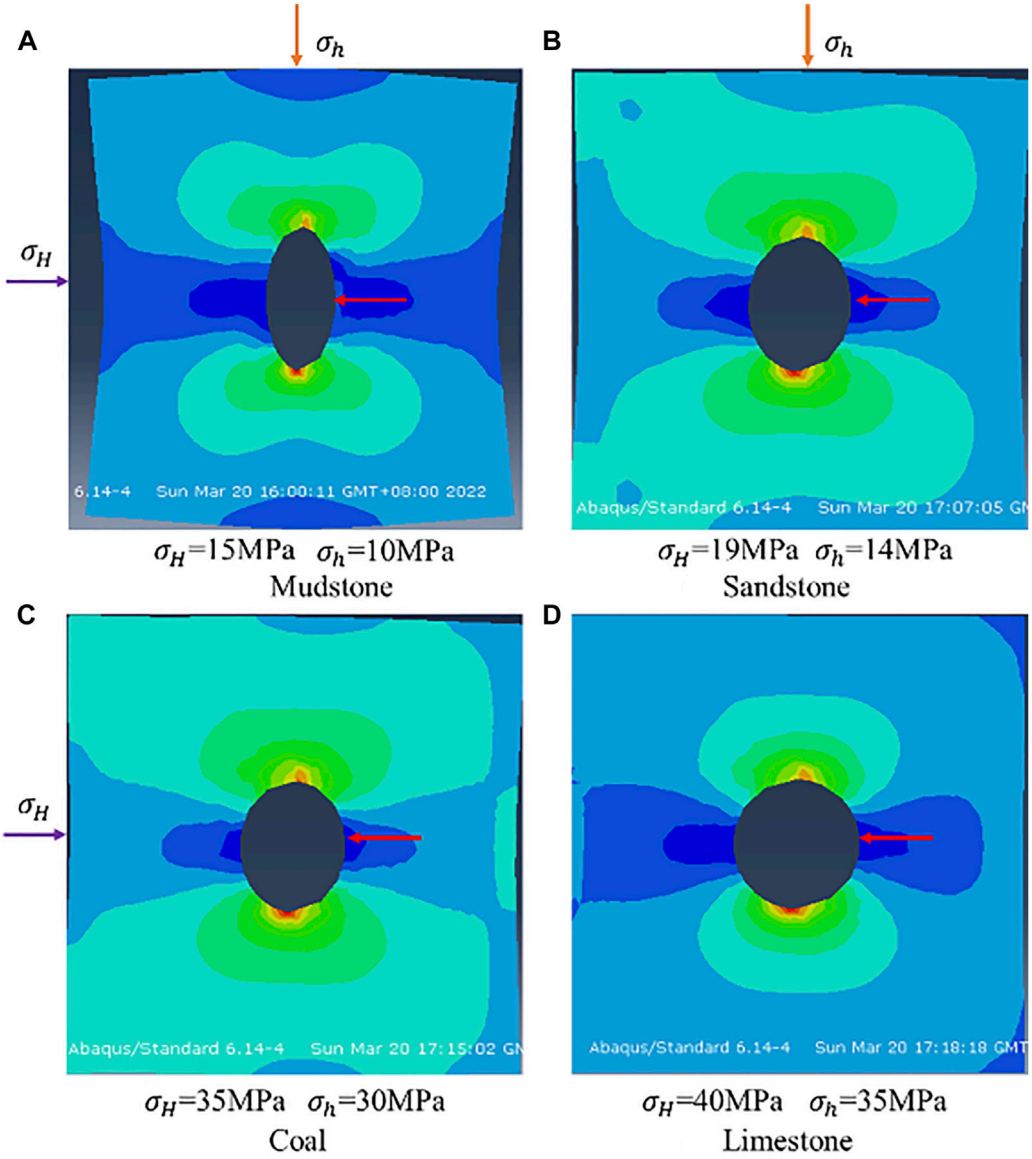

FIGURE 11
Numerical simulation of the borehole morphology of different lithologies under *in situ* stress.

horizontal principal stress difference ($\sigma_H - \sigma_h$) is low in the east and high in the west, with the lowest value of 1.8 MPa. The horizontal principal stress difference ($\sigma_H - \sigma_h$) is negatively correlated with the daily gas production, with a limit of 5 MPa. When the horizontal principal stress difference ($\sigma_H - \sigma_h$) is lower than 5 MPa, it is a high-yield gas area. Therefore, it can be seen that the high-yielding gas area of the No. 3 coal seam is mainly distributed in the west of the study area, while the horizontal principal stress difference ($\sigma_H - \sigma_h$) of the No. 15 coal seam in the northeast of the study area is greater than 5 MPa; thus, this area is a low-yielding gas area.

5 Discussion

5.1 Analysis of applicability of the new method

Generally, without the interference of external factors, the three-dimensional *in situ* stress in the crust is in the equilibrium state. When the formation is drilled, the *in situ* stress around the borehole will be changed rapidly, breaking the original *in situ* stress balance and then redistributing. Owing to the existence of horizontal differential stress in the formation, the stress concentration in the borehole wall leads

10.3389/feart.2022.961311

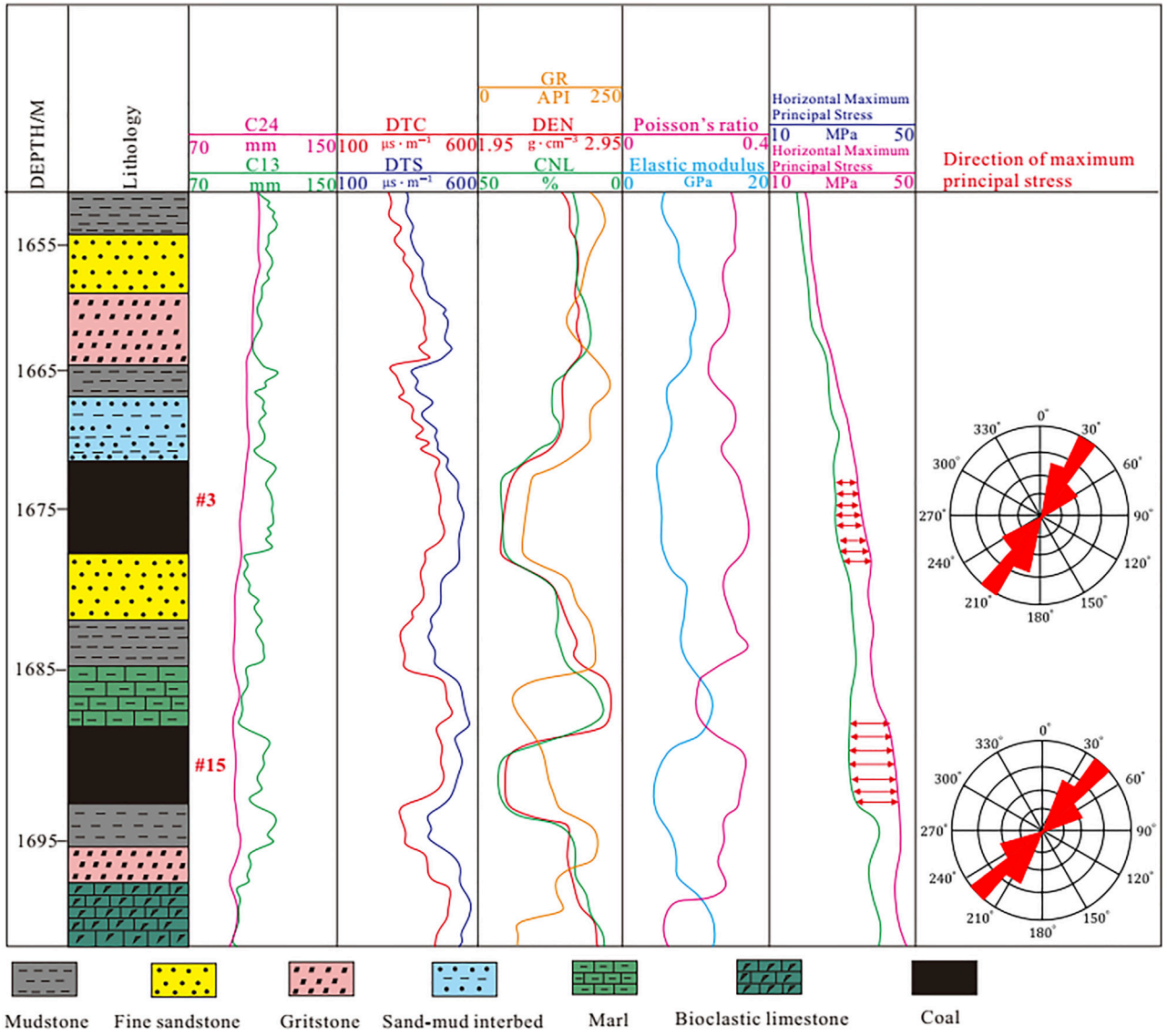

FIGURE 12
In situ stress prediction profile of well S16.

TABLE 2 Direction of the long axis of ellipse and maximum principal stress.

Depth(m)	Direction of the long axis of ellipse (°)	Direction of the maximum principal stress (°)
1,658.5	307.5	29
1,666.8	310.1	30.8
1,675.3	318.7	31.5
1,680.8	305.9	30.2
1,690.5	302.7	30.5

to deformation of the borehole. Theoretical derivation shows that the geometric morphology equation of borehole deformation under stress is an elliptic equation, namely, the borehole shape under stress is ellipse. Thus, the quasi-elliptic shape structure of the deformation of the shaft wall under *in situ* stress is applied to calculate the *in situ* stress. Numerical simulation shows that the borehole shape of different types of rocks tends to be a quasi-elliptic shape structure under the *in situ* stress, which is consistent with theoretical deduction. The direction of the maximum horizontal principal stress is parallel to the short axis of

TABLE 3 Contrast between prediction by the new method and test by acoustic emission.

Lithology	Number	Maximum horizontal stress/MPa			Minimum horizontal stress/MPa		
		Prediction	Test	Error/%	Prediction	Test	Error/%
Mudstone	S-M-1	18.7	19.8	5.50	14.5	15.9	8.80
	S-M-2	20.1	22.1	8.20	17.6	19.5	8.72
	S-M-3	21.6	22.7	4.73	19.8	17.1	8.69
	S-M-4	22.1	20.2	8.50	20.3	18.5	8.78
	S-M-5	22.6	21.7	3.46	20.8	19.3	7.21
Fine sandstone	S-F-1	23.7	22.8	3.79	20.9	19.9	4.75
	S-F-2	24.9	25.3	1.59	21.1	22.1	4.50
	S-F-3	25.1	25.9	3.08	22.8	23.9	4.60
	S-F-4	25.2	26.1	3.44	23.1	23.7	2.53
	S-F-5	24.7	25.6	3.51	22.2	22.9	0.87
Gritstone	S-G-1	25.7	26.3	2.28	22.7	21.9	3.52
	S-G-2	25.9	26.1	0.77	22.1	22.5	1.78
	S-G-3	26.1	26.4	1.13	23.3	22.9	1.72
	S-G-4	26.5	27.1	2.21	23.4	23.0	1.71
	S-G-5	26.8	25.8	3.73	23.7	23.1	2.53
Coal	S-C-1	27.5	28.2	2.50	25.0	25.2	0.80
	S-C-2	28.1	28.5	1.41	26.2	26.7	1.87
	S-C-3	29.6	28.8	2.70	25.7	23.9	7.00
	S-C-4	32.1	32.3	0.62	29.9	30.7	3.11
	S-C-5	33.2	33.7	1.50	30.1	30.5	1.31
Limestone	S-L-1	35.1	35.8	2.00	31.9	32.5	1.85
	S-L-2	36.3	37.1	2.16	32.7	33.8	3.26
	S-L-3	36.7	37.5	2.13	33.1	34.3	3.50
	S-L-4	38.9	39.2	0.78	35.4	36.2	2.20
	S-L-5	40.8	41.9	2.63	33.9	32.9	2.95

ellipse, while the direction of the minimum horizontal principal stress is parallel to the long axis of the ellipse.

For the same lithology, the degree of borehole ellipticity depends on the maximum and minimum horizontal principal stress σ_H and σ_h . When $\sigma_H/\sigma_h = 1$, regardless of the absolute value of σ_H or σ_h , the borehole will not deform. When $1 < \sigma_H/\sigma_h < 3$, the borehole will be elliptically deformed under the horizontal principal stress difference. This is a necessary condition for the ovalization of a circular wellbore. If the absolute values of σ_H and σ_h are large and the rock strength is low, the elliptical deformation is obvious within the range of compressive strength. Alternatively, when $\sigma_H/\sigma_h > 3$, the wellbore will collapse and tend to be irregular.

The softer the stratum is, the more elliptical the borehole shape structure becomes under the action of stress. Therefore, the elliptical shape of mudstone under the action of stress is the most prominent among the five types of rocks: mudstone, fine sandstone, gritstone, coal, and limestone. The measurement of borehole diameter is conducted by the formation dip angle and four-wall borehole diameter logging instrument. The downhole measuring device consists of four measuring arms, 1–3 and 2–4, which are perpendicular to each other, located in the same plane and in close contact with the borehole wall. When the logging cable is raised from the bottom of the hole, the device rotates at a rate in the hole, with C13 corresponding to the long axis of the elliptical hole and C24 corresponding to the short axis of the elliptical hole. Consequently, the borehole shape structure can be measured to predict the formation stress.

The method proposed in this study is applied to coal measure strata in Qinshui Basin, which are mainly composed of

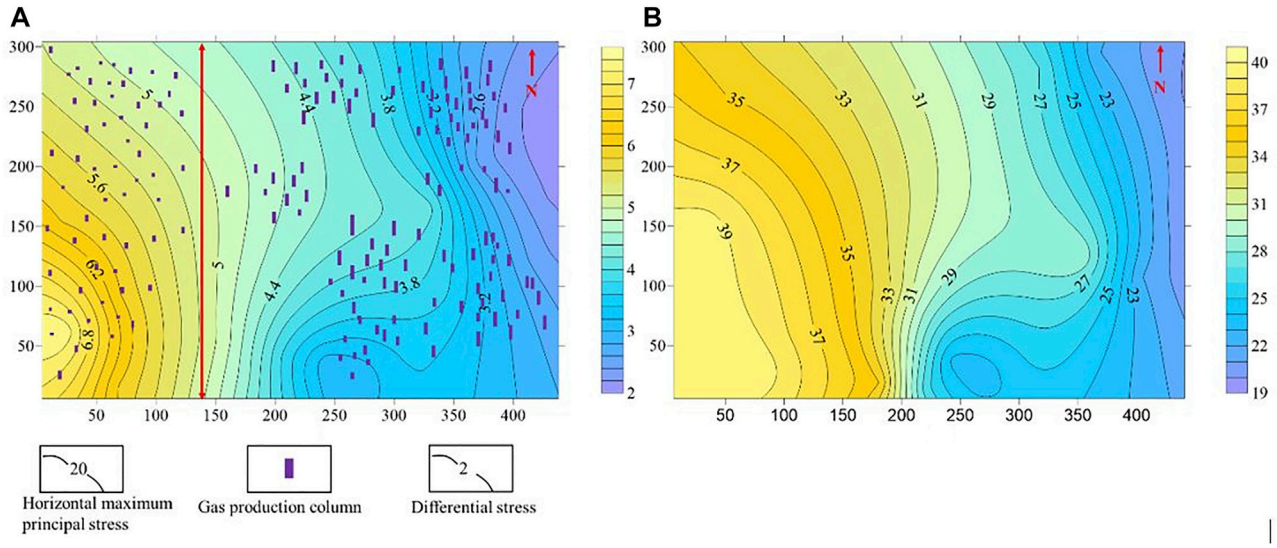

FIGURE 13
Distribution of the maximum horizontal principal stress, horizontal principal stress difference ($\sigma_H - \sigma_h$), and gas producing column of the No. 3 coal seam.

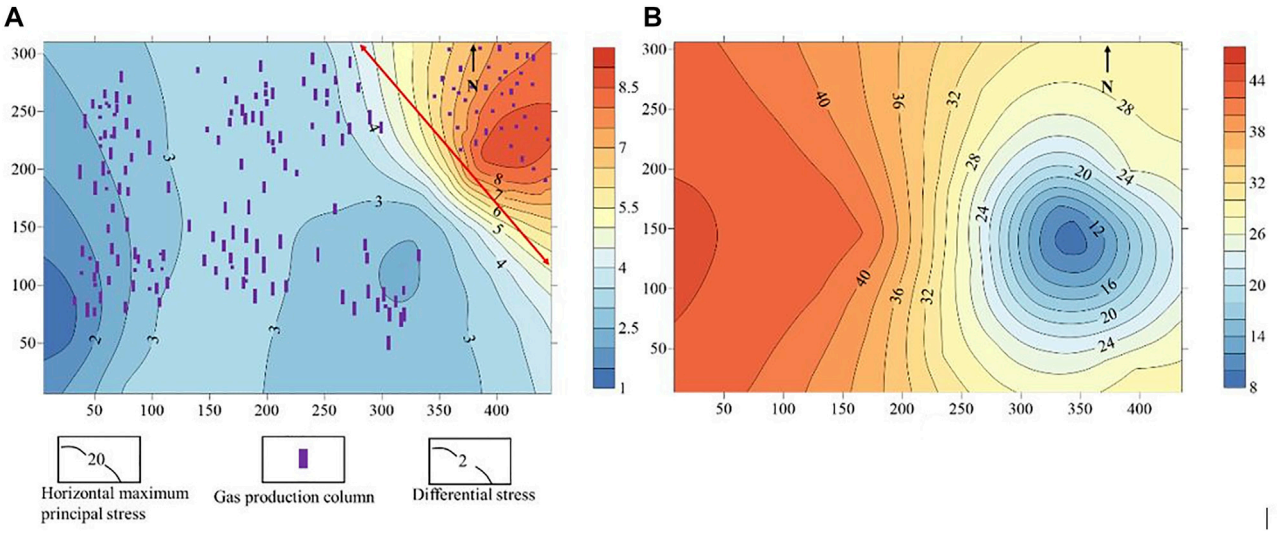

FIGURE 14
Distribution of the maximum horizontal principal stress, horizontal principal stress difference ($\sigma_H - \sigma_h$), and gas producing column of the No. 15 coal seam.

mudstone, fine sandstone, gritstone, coal, and limestone. By comparing the *in situ* stress predicted by the new method with the ones measured by the acoustic emission method, it is revealed that the overall error is less than 9%, which meets the actual needs of the production. Among these five lithologies, the accuracy of the maximum and minimum horizontal principal stress of coal is the highest, with an error of 2.01 and 2.56%, respectively, followed by fine sandstone, gritstone, and limestone, and the accuracy of the maximum and minimum horizontal principal stress of mudstone is the lowest. Although the borehole structure of mudstone is more elliptic under stress, mudstone easily expands with low strength when exposed to water. Hence,

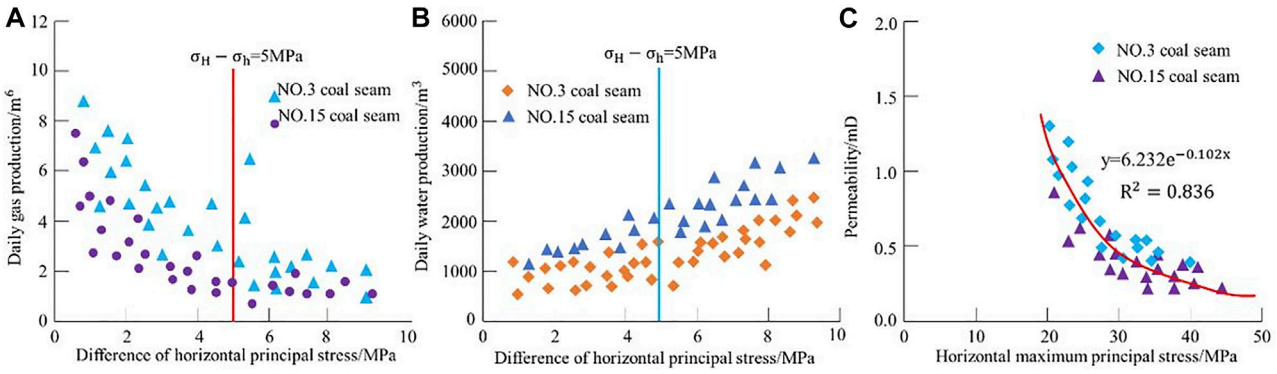

FIGURE 15
Relationship between the horizontal principal stress and daily gas volume, daily water volume, and permeability.

the instrument will meet much difficulty in the process of pushing in the mudstone, resulting in measurement errors. As mudstones are softer, some of the elliptic deformation of mudstone is owing to hydration expansion rather than stress, which increases the prediction error. Compared with fine sandstone, gritstone, and limestone, the hardness of coal is relatively soft and its strength is relatively low; in addition, its swelling effect is not obvious when it is exposed to water. However, the deformation of the coal seam borehole is mainly due to the *in situ* stress. Consequently, more accurate *in situ* stress data can be achieved by measuring the borehole shape structure of the coal seam. Due to the large hardness of limestone is very large, although the hydration expansion effect is very weak, the limestone borehole will have obvious deformation caused by the *in situ* stress in the deeper strata with great *in situ* stress. Therefore, the prediction method of *in situ* stress based on the borehole deformation proposed in this study is applicable for deep coal measure strata.

5.2 Sensitivity analysis of coal seam permeability to *in situ* stress

Permeability of the coal seam is sensitive to *in situ* stress. It can be seen from Figure 15C that the permeability and maximum principal stress of the coal seam decrease exponentially. The *in situ* stress of the coal seam usually increases with the depth. Affected by the *in situ* stress, the opening of pore fissure is difficult and the connectivity is adversely affected, thereby decreasing the permeability, which is not conducive to the production of coalbed methane, resulting in reduction of gas production.

Owing to the difference of regional *in situ* stress, the permeability difference between the No. 3 coal seam and No. 15 coal seam in the study area is obvious. The horizontal principal stress of the No. 15 coal seam is generally greater than that of the No. 3 coal seam; correspondingly, the corresponding permeability of the No. 15 coal seam is less than that of the No. 3 coal seam. The higher the permeability, the more favorable the gas flow. According to Figure15A, it can be illustrated that the daily gas flow of the No. 3 coal seam is greater than that of the No. 15 coal seam. The high *in situ* stress makes the pore structure of the No. 15 coal seam worse, which is a factor causing the low daily gas flow of the No. 15 coal seam.

Permeability affects the productivity of CBM of a single well. The correlation analysis between the horizontal principal stress difference ($\sigma_H - \sigma_h$) and the daily gas and water volume of a single well exhibits that the daily gas volume is negatively correlated with the horizontal principal stress difference ($\sigma_H - \sigma_h$), while the daily water volume is positively correlated with the horizontal principal stress difference. When the stress difference of the coal seam is small, the stress in the rock is more uniform; moreover, the pore space is easier to open. Adversely, the pore space, especially the fissure, in the rock is easy to close. It can be exhibited that the smaller the *in situ* stress difference is, the higher the productivity of the coalbed methane well is, which is consistent with Figures 13 and 14. It can be seen from Figure15A that when the horizontal principal stress difference ($\sigma_H - \sigma_h$) is less than 5MPa, the daily gas volume is more than 1000 m^3, while when the horizontal principal stress difference ($\sigma_H - \sigma_h$) is more than 5MPa, the daily gas volume is less than 1000 m^3. The horizontal principal stress difference ($\sigma_H - \sigma_h$) affects the fracturing effect of coalbed methane. The larger the horizontal principal stress difference ($\sigma_H - \sigma_h$) is, the stronger the longitudinal penetration capacity of pressure fracture is. The horizontal principal stress difference of the No. 15 coal seam is greater than that of the No. 3 coal seam. The fracture of the No. 15 coal seam runs through the adjacent water layer, increasing the hydraulic fracture height of upper and lower seams, resulting in serious escape loss of single-well

gas production and sharp increase of water production. Consequently, the daily gas production of the No. 3 coal seam is greater than that of the No. 15 coal seam, while the corresponding water production is lower than that of the No. 15 coal seam. In the coal seam area with a high principal stress difference value, it is suggested to adopt small-scale plugging to re-fracturing, namely, fracturing with small fluid volume, small displacement, and low sand intensity.

6 Conclusion

1) Based on the theory of elasticity, this study deduces the geometric morphology equation of a borehole under the action of *in situ* stress. We verified that the borehole shape under *in situ* stress is a quasi-elliptic structure through numerical simulation and evaluated the feasibility of the method of predicting *in situ* stress with quasi-elliptic geometric parameters.
2) The DTS was sensitive to the DTC, GR, and DEN logging parameters. Based on the sensitive logging parameters, the predicted DTS with a multi-layer feedforward ANN is significantly in line with the measured values, which provides accurate rock mechanical parameters for *in situ* stress prediction.
3) The comparison between the *in situ* stress prediction of the coal measure strata by the new method and the acoustic emission test shows that the average error of the maximum and minimum horizontal principal stresses predicted by the new method is less than 9.2%, which meets the production demand. Compared with the prediction results of mudstone, fine sandstone, gritstone, and limestone, the new prediction method achieved the smallest average error in the coal seam, whose value was 2.15%.
4) The gas production of CBM wells in the study area is highly correlated with the distribution law of *in situ* stress. The maximum horizontal principal stress and horizontal principal stress difference were inversely proportional to the daily gas production. When the horizontal principal stress difference was less than 5 MPa, the daily gas production was more than 1,000 m^3; otherwise, it was less than 1,000 m^3. The No. 3 coal seam presents a high-yield gas area west of the study area, while the No. 15 coal seam presents a high-yield gas area east of the study area.

Data availability statement

The raw data supporting the conclusions of this article will be made available by the authors, without undue reservation.

Author contributions

XF completed the conception, design of structure, writing, revision, acquisition and analysis of data. HF completed the revision of some figures and improvements of language and actual application. YW completed the revision of theory and numerical simulation and the final approval of the version to be published. TF completed the revision of method and update of data.

Funding

Funding was supported by the National Natural Science Fund of China (51974332), the Key Basic Research Program of Natural Science of Shannxi Province [2022JZ-16], and the Key Top-level Design Program of the Major Project of Science and Technology Innovation and Entrepreneurship Foundation of Tiandi Technology Co., Ltd. [2020-TD-ZD003].

Acknowledgments

I acknowledge the suggestion of my co-authors.

Conflict of interest

The authors declare that the research was conducted in the absence of any commercial or financial relationships that could be construed as a potential conflict of interest.

Publisher's note

References

Atsushi, M., Tsuneo, Y., Hiroshi, I., and Matsumoto, S. (2007). *In-situ* stress measurement by the stress relief technique using a multi-component borehole instrument. *Earth Planets Space* 59, 133–139. doi:10.1186/bf03352686

Behzad, M., Hossein, I., and Memarian, H. (2019). Shear wave velocity prediction using Elman artificial neural network. *Carbonates Evaporites* 34, 1281–1291. doi:10.1007/s13146-017-0406-x

Bell, J. S. (2006). *In-situ* stress and coal bed methane potential in Western Canada. *Bull. Can. Pet. Geol.* 54, 197–220. doi:10.2113/gscpgbull.54.3.197

Cai, M. F., Chen, C. Z., and Peng, H. (2006). *In-situ* stress measurement by hydraulic fracturing technique in deep position Wanfu coal mine. *Chin. J. Rock Mech. Eng.* 25, 1069–1074.

Daniel, G., and Christoph, B. (2016). *In-situ* stress measurement and prediction of stresses and strain during casting of steel. *Metallurgical Mater. Trans.* 6, 1–19. doi:10.1007/s11661-015-3184-x

Deng, G. T., Ma, N. J., and Jia, M. K. (2006). Application of artificial neural network in identifying lithology of roadway strata. *J. Min. Saf. Eng.* 23, 182–188.

Fang, X. X., Feng, H., and Wang, H. (2022). Study on intelligent prediction method of rock drillability based on Bayesian lithology classification and optimized BP neural network. *Petroleum Sci. Technol.* 40, 2141–2162. doi:10.1080/10916466.2022.2036759

Farshid, M., Mohammad, A. R., and Hamed, G. M. (2020). Prediction of *in situ* stresses, mud window and overpressure zone using well logs in South Pars field. *J. Pet. Explor. Prod. Technol.* 10, 1869–1879. doi:10.1007/s13202-020-00890-9

Feng, J. W., Shang, L., Li, X. Z., and Luo, P. (2019). 3D numerical simulation of heterogeneous *in situ* stress field in low-permeability reservoirs. *Pet. Sci.* 16, 939–955. doi:10.1007/s12182-019-00360-w

Fu, X. L., Dai, J. S., and Zhang, D. D. (2017). Prediction of fractures of seam No.3 in northern Shizhuang Qinshui basin. *Coal Geol. Exploration* 1, 56–63.

Haison, B. C., and Herrick, C. G. (1985). "*In-situ* stress evaluation from borehole breakouts: experimental studies," in 26th US symposium on rock mechanics, Rapid City, CD, 1985, 1207–1218.

Hikweon, L., and See, H. O. (2018). Estimation of *in situ* stresses with hydro-fracturing tests and a statistical method. *Rock Mech. Rock Eng.* 51, 779–799. doi:10.1007/s00603-017-1349-1

Huffman, K. A., Saffer, D. M., and Dugan, B. (2016). *In situ* stress magnitude and rock strength in the nankai accretionary complex: a novel approach using paired constraints from downhole data in two wells. *Earth Planets Space* 68, 123–132. doi:10.1186/s40623-016-0491-4

Husken, M., Jin, Y., and Sendhoff, B. (2005). Structure optimization of neural networks for evolutionary design optimization. *Soft Comput.* 9, 21–28. doi:10.1007/s00500-003-0330-y

Ishida, T., and Saito, T. (1995). Observation of core discing and *in situ* stress measurements; stress criteria causing core discing. *Rock Mech. Rock Eng.* 28, 167–182. doi:10.1007/bf01020150

Jaeger, C. J., Neville, G. W. C., and Robert, Z. R. (2009). *Fundamentals of rock mechanics*. UK: John Wiley & Sons.

Ju, W., Niu, X. B., Feng, S. B., You, Y., Xu, K., Wang, G., et al. (2020). Predicting the present-day *in situ* stress distribution within the Yanchang formation Chang 7 shale oil reservoir of Ordos Basin, central China. *Pet. Sci.* 17, 912–924. doi:10.1007/s12182-020-00448-8

Ju, W., Shen, J., Qin, Y., Meng, S., Li, C., Li, G., et al. (2017). *In-situ* stress distribution and coalbed methane reservoir permeability in the Linxing area, eastern Ordos Basin, China. *Front. Earth Sci.* 12, 545–554. doi:10.1007/s11707-017-0676-6

Khair, D., Cooke, M., and Hand, M. (2013). The effect of present day *in situ* stresses and paleo-stresses on locating sweet spots in unconventional reservoirs, a case study from Moomba-Big Lake fields Cooper Basin South Australia. *J. Petroleum Explor. Dev.* 3, 207–221. doi:10.1007/s13202-013-0082-x

Kirsch, G. (1898). *Die theorie der elastizitat und die bedürfnisseder festigkeitslehre*, 42. UK: Veit Ver Deut Ing, 797–807.

Lin, L., Wang, J., and Liu, X. J. (2021). Prediction for permeability of tight reservoir based on artificial neural network. *Well Logging Technol.* 45, 179–183. doi:10.16489/j.issn.1004-1338.2021.02.012

Liu, B., Huang, W. H., and Ao, W. H. (2014). Adsorption capacity of high-rank coal and its influencing factors: taking shizhuang block of Qinshui basin as an example. *J. Xi'an Shiyou Univ. Nat. Sci. Ed.* 29, 31–41.

Liu, S. S., Peng, G. X., and Yin, G. M. (2021). A study on the *in-situ* stress conditions at the Kailuan mining area in China and their influence on coal mine water inrush. *Arab. J. Geosci.* 14, 2057–2066. doi:10.1007/s12517-021-08276-9

Lv, J., Xie, R. C., and Zhou, W. (2017). Application of LM-BP neural network in simulation of shear wave velocity of shale formation. *J. China Univ. Pet.* 41, 75–83. doi:10.3969/j.issn.1673-5005.2017.03.009

Peska, P., and Zoback, M. D. (1995). Compressive and tensile failure of inclined wellbores and determination of *in-situ* stress and rock strength. *J. Geophys. Res.* 100, 12791–12811. doi:10.1029/95jb00319

Shi, X. H., Zhang, J. X., and Li, Q. G. (2021). Characteristics of *in situ* stress field in the Huainan mining area, China and its control factors. *Environ. Earth Sci.* 80, 682–700. doi:10.1007/s12665-021-09991-y

Wang, C. L., and Zhang, X. D. (2018). Distribution rule of the *in-situ* stress state and its influence on the permeability of a coal reservoir in the southern Qinshui Basin, China. *Arab. J. Geosci.* 11, 586–595. doi:10.1007/s12517-018-3938-z

Wang, J., Kang, Y. S., and Jiang, B. Y. (2017). Difference of CBM development conditions in Shouyang and Shizhuang blocks, Qinshui basin. *Coal Geol. Exploration* 4, 57–62.

Wang, L. J., and Pan, L. Z. (1991). *Crustal stress measurements and their application in engineering*. Beijing: Geological Publishing House, 1–31.

Wu, H., Zhao, M., Zhuo, Q., Lu, X., Wang, L., Li, W., et al. (2020). The effect of salt on the evolution of a subsalt sandstone reservoir in the Kuqa foreland basin, Western China. *Carbonates Evaporites* 35, 72–12. doi:10.1007/s13146-020-00604-6

Xu, L. Q., Shi, M. C., and Meng, Y. F. (2016). Analysis on the stress distribution of elliptic borehole in gas drilling. *Drilling Production Technol.* 39, 43–47.

Yang, B. B., He, M. M., Zhang, Z. Q., Zhu, J., and Chen, Y. (2022). A new criterion of strain rock burst in consideration of the plastic zone of tunnel surrounding rock. *Rock Mech. Rock Eng.* 55, 1777–1789. doi:10.1007/s00603-021-02725-3

Yang, D. H., Ning, Z. X., Li, Y. M., Lv, Z., and Qiao, Y. (2021). *In-situ* stress measurement and analysis of the stress accumulation levels in coal mines in the northern Ordos Basin, China. *Int. J. Coal Sci. Technol.* 8, 1316–1335. doi:10.1007/s40789-021-00407-7

Zhang, H., Ju, W., Xu, K., Huang, P., Zhong, Y., Liu, X., et al. (2021). Present-day *in situ* stress prediction in bozi 3 deep sandstone reservoir, kuqa depression: implications for gas development. *Arab. J. Geosci.* 14, 1434–1444. doi:10.1007/s12517-021-07847-0

Zhang, Y., Zhong, H. R., Wu, Z. Y., Zhou, H., and Ma, Q. Y. (2020). Improvement of petrophysical workflow for shear wave velocity prediction based on machine learning methods for complex carbonate reservoirs. *J. Pet. Sci. Eng.* 192, 107234. doi:10.1016/j.petrol.2020.107234

Zoback, M. D., Moos, D., Mastin, L., and Anderson, R. N. (1985). Well bore breakouts and *in situ* stress. *J. Geophys. Res.* 90, 5523–5530. doi:10.1029/jb090ib07p05523

Zou, D. H., and Kaiser, P. K. (1990). Determination of *in situ* stresses from excavation-induced stress changes. *Rock Mech. Rock Eng.* 23, 167–184. doi:10.1007/bf01022952